remote sensing

MDPI

Article

Wind Profile Retrieval Based on LSTM Algorithm and Mobile Observation of Brightness Temperature over the Tibetan Plateau

Bing Chen [1], Xinghong Cheng [2,*], Debin Su [1], Xiangde Xu [2], Siying Ma [1] and Zhiqun Hu [2]

[1] College of Electronic Engineering, Chengdu University of Information Technology, Chengdu 610225, China; chenbing910228@163.com (B.C.); masiying950831@163.com (S.M.)
[2] State Key Lab of Severe Weather, Chinese Academy of Meteorological Sciences, Beijing 100081, China; huzq@cma.gov.cn (Z.H.)
* Correspondence: cxingh@cma.gov.cn

Abstract: Stationary or mobile microwave radiometers (MRs) can measure atmospheric temperature, relative humidity, and water vapor density profiles with high spatio-temporal resolution, but cannot obtain the vertical variations of wind field. Based on a dataset of brightness temperatures (TBs) measured with a mobile MR over the Three-River-Source Region of the Tibetan Plateau from 18 to 30 July 2021, we develop a direct retrieval method for the wind profile (WP) based on the Long Short-Term Memory (LSTM) network technique, and obtain the reliable dynamic variation characteristics of the WP in the region. Furthermore, the ground-based radiative transfer model for TOVS (RTTOV-gb) was employed to validate the reliability of the TB observation, and we analyzed the impact of weather conditions, altitude, observational mode, and TB diurnal variation on the accuracy of the TB measurement and the retrieval of the WP. Results show that the TB from the mobile observation (MOTB) on clear and cloudy days are close to those of the simulated TB with the RTTOV-gb model, while TB measurements on rainy days are far larger than the modeled TBs. When compared with radiosonde observations, the WPs retrieved with the LSTM algorithm are better than the ERA5 reanalysis data, especially below 350 hPa, where the root mean square errors for both wind speed and wind direction are smaller than those of ERA5. The major factors influencing WP retrieval include the weather conditions, altitude, observational mode, and TB diurnal variation. Under clear-sky and cloudy conditions, the LSTM retrieval method can reproduce the spatio-temporal evolution of wind field and vertical wind shear characteristics. The findings of this study help to improve our understanding of meso-scale atmospheric dynamic structures, characteristics of vertical wind shear, atmospheric boundary layer turbulence, and enhance the assessment and forecasting accuracy of wind energy resources.

Keywords: wind profile retrieval; LSTM algorithm; microwave radiometer; mobile observation; brightness temperatures

Citation: Chen, B.; Cheng, X.; Su, D.; Xu, X.; Ma, S.; Hu, Z. Wind Profile Retrieval Based on LSTM Algorithm and Mobile Observation of Brightness Temperature over the Tibetan Plateau. *Remote Sens.* **2024**, *16*, 1068. https://doi.org/10.3390/rs16061068

Academic Editor: Mark Bourassa

Received: 1 February 2024
Revised: 12 March 2024
Accepted: 13 March 2024
Published: 18 March 2024

1. Introduction

The Tibetan Plateau (TP) is the world's largest plateau, with the highest altitude and the most complex topography. The TP is referred to as the 'Asian Water Tower', which means the sources of major rivers such as the Yellow River, Yangtze River, and Lancang River (the Three-River-Source Region, TRSR) [1]. The dynamic and thermal effects generated by large topography have an important impact on weather and climate, atmospheric circulation, water, and energy cycles in China and around the globe [2–15]. However, due to the complicated topography, inconvenient transportation, and challenges associated with the maintenance of measurement equipment, surface meteorological and radiosonde stations over the TP are sparse, which leads to an insufficient understanding of the atmospheric dynamic and thermal structure [5,7,15]. There are only 15 radiosonde stations over the TP and, at present, two observations are made every day, at 00:00 and 12:00 UTC. In

order to make up for the shortage of low-density conventional radiosonde observations (Raobs) and their low time-frequency, microwave radiometers (MRs) are widely used in aerological sounding. Ground-based MR (GMR), as a typical form of passive remote sensing equipment, can measure the brightness temperature (TB) data for downward radiation at 22–30 GHz and 51–59 GHz bands. The atmospheric temperature (AT), relative humidity (RH), and water vapor density (WVD) profiles can be retrieved by using the measured TB data. MRs have been widely applied to the continuous observational research of AT, RH, and WVD profiles under any weather conditions [16,17]. MRs can capture the fine thermodynamic structure of meso-scale convective systems and have become a valuable supplement to routine Raobs [18,19].

Most research uses GMR for field experiments and operational applications with a fixed observation mode, which can obtain the AT, RH, and WVD profiles at one site, but it cannot quickly and effectively capture the spatio-temporal variational characteristics of the atmospheric vertical structure in a wide range. The feasibility and reliability of mobile observation (MO) using airborne, vehicle-mounted, shipborne, and satellite-based MRs are discussed in a few research studies [20]. Serafin et al. [21] proposed that aircraft equipped with an MR could effectively investigate meso-scale convective systems; Huggins et al. [22] successfully applied a vehicle-mounted MR observation system to study the monsoon storm in the central Wasatch Plateau of Utah, USA, and studied the spatial distribution characteristics of supercooled liquid water in a mountainous winter storm. Karan et al. [23] applied a vehicle-mounted mobile integrated observation system including MRs, wind profile (WP) radars, altimeters, and ground observation equipment to conduct field experiments in the Midwest of the United States and obtain characteristics of vertical wind shear. Some studies adopted shipborne [24] and space-based MR [25] data to examine the spatio-temporal variation of atmospheric precipitable water and cloud liquid water (CLW) content. Recently, Cheng et al. [26] carried out the first Mobile Field Observation Campaign of Atmospheric Profiles (MFOCAP) from 18 to 30 July 2021 in southeast Tibet and the TRSR by adopting two vehicle-mounted integrated MO systems, which are equipped with an MR and other instruments. They acquired reliable MO datasets including atmospheric AT, RH, and WVD profiles, with high temporal-spatial resolution. Furthermore, the MO temperature profile data were assimilated into the Global Forecast System of China Meteorological Administration (CMA_GFS) model, and the improvement of rainfall prediction over the TP was evaluated.

In general, from MR-measured TB data, the retrieval of AT, RH, and WVD profiles is performed with reliable quality. The retrieval of WP may not be possible through conventional methods. With the rapid development of artificial intelligence technologies, the direct retrieval of wind field information from MR observational data is feasible. Bu et al. [27] employed an enhanced deep learning network to inverse global sea surface wind speed (WS) from GNSS-R data, although the continuity and spatial correlation of the wind field were not taken into account. Shi et al. [28] and Ouyed et al. [29] considering the characteristics of the wind field, established a field-to-field sea surface wind field inversion model based on deep learning. Ma et al. [30] utilized a neural network approach and TB data observed by geosynchronous infrared hyperspectral sounders to retrieve WP information during the Maria typhoon process. Whereas this method can't retrieve the wind field information below clouds. GMR with the bottom-up detection approach, compensates for the satellite's inability to capture wind field information under cloud [31]. Considering the continuity and consistency of wind field and combining the long short-term memory capabilities of Long Short-Term Memory (LSTM) algorithm [32], this paper developed a WP inversion method based on LSTM algorithm and TB from mobile observation (MOTB) data from the MFOCAP over the TRSR. This method can inverse reliable WP information and provides an effective pathway to enhance our understanding of the vertical dynamic structure.

Following this introduction, Section 2 introduces the LSTM algorithm and dataset. Evaluations of the reliability of MOTB data using the ground-based radiative transfer model for the TOVS (RTTOV-gb) model are reported in Section 3. Section 4 assesses the

inversion accuracy of WP, and analyzes the impact factors and variation characteristics of vertical wind shear. Conclusions and discussions are given in Section 5.

2. Data and Methods

We referred to the physical basis of WP inversion presented by Ma et al. [30]. They mentioned that, under cloudy skies, the visible and longwave infrared (IR) band radiances can be used to track cloud motion-based vectors, while in clear skies, water vapor-sensitive band radiances are used to track moisture features for motion vectors of water vapor molecules. The microwave radiation in the band of 22.35–30 GHz is sensitive to water vapor changes at different altitude layers, and is the preliminary source of information for tracking moisture-based WPs. The vehicle-mounted microwave radiometer measured the AT and moisture profile information from 18 to 30 July 2021 in the TRSR, and obtained a reliable TB dataset with high temporal and spatial resolution. The motion vector information of water vapor and oxygen molecules in the TRSR is presented by the TB data, and the LSTM algorithm can use the motion vector information to retrieve the WP. Because the TB at 22 channels can represent the wind field information at different layers, we only use the TB at 22 channels as the input for the WP inversion model.

2.1. Study Area

The TRSR is located in the south of Qinghai Province and is the source of the Yangtze, Yellow, and Lancang rivers. It is also known as "China's Water Tower", and is highly sensitive to climate change. The average elevation of TRSR is larger than 4000 m, the average annual temperature falls between −5.6 and −3.8 °C, and the annual precipitation is 262.2 to 772.8 mm from west to southeast [33]. The climate of TRSR has changed, with precipitation and temperature increasing at rates of 6.653 to 10.31 (mm/10a) and 0.33 (°C/10a) over the past few decades, respectively [34,35]. The RH and WS in the TRSR decreased from 1960 to 2009 [36].

2.2. Dataset

When training the WP inversion model, we used observed TB data, measured with the GMR at Mangai (MA) Station (38°25′N, 90°E; 2947 m a.s.l., Figure 1) in Qinghai Province from January to December 2021, and the matching ERA5 reanalysis WP data as the independent and dependent variables of the training model. In order to obtain the WP information in the study area, the MOTB data from 18 to 30 July 2021 were used as the input to the WP inversion model. Due to the short duration of MO, the MOTB has only 301 sets of data after spatio-temporal matching with the ERA5 reanalysis data, which is not enough to construct the WP inversion model. Therefore, the observed TB data from January to December 2021 at MA station, which is nearest to the MO route, were selected to construct training sets, while the MOTB data were used as testing sets.

The MA GMR station is the closest to the MO route in the TRSR among all GMR stations over the TP [37,38]. The two MRs (model.MWP967KV) used at the MA station and the MO field experiment are the same, both produced by the Xi'an Electronic Engineering Research Institute in China. This instrument is capable of continuously measuring the variation characteristics of TB for downward radiation at water vapor and oxygen absorption channels, which comprise 8 channels in the K band (22–30 GHz) and 14 channels in the V band (51–59 GHz). Each channel's center frequency is listed in Table 1. The sampling frequency was set to 2 min, and we obtained 237,990 sets of TB data in total.

TB data observed during the MFOCAP over the TRSR from 18 to 30 July 2021 (as shown in Figure 1) were used as the input features of the testing set. The data from the MFOCAP were divided into four stages, with each stage spanning three days of a circling journey in the TRSR: Xining (XN) → Dari (DR) → Yushu (YS) → XN cites. The average elevation of the MO route was above 3500 m. The MO system passed by the Yangtze and Yellow River, and approached the Lancang River. A total of 11,086 sets of valid TB data

were collected. Detailed information about the MFOCAP was described in the reference by Cheng et al. [26].

Table 1. Center frequencies of 22 channels of MR.

K-Band			V-Band		
Number	**Center Frequency**	**Channel Number**	**Center Frequency**	**Channel Number**	**Center Frequency**
1	22.235 GHZ	9	51.250 GHZ	16	54.940 GHZ
2	22.500 GHZ	10	51.760 GHZ	17	55.500 GHZ
3	23.035 GHZ	11	52.280 GHZ	18	56.020 GHZ
4	23.835 GHZ	12	52.800 GHZ	19	56.660 GHZ
5	25.000 GHZ	13	53.340 GHZ	20	57.290 GHZ
6	26.235 GHZ	14	53.850 GHZ	21	57.960 GHZ
7	28.000 GHZ	15	54.400 GHZ	22	58.800 GHZ
8	30.000 GHZ				

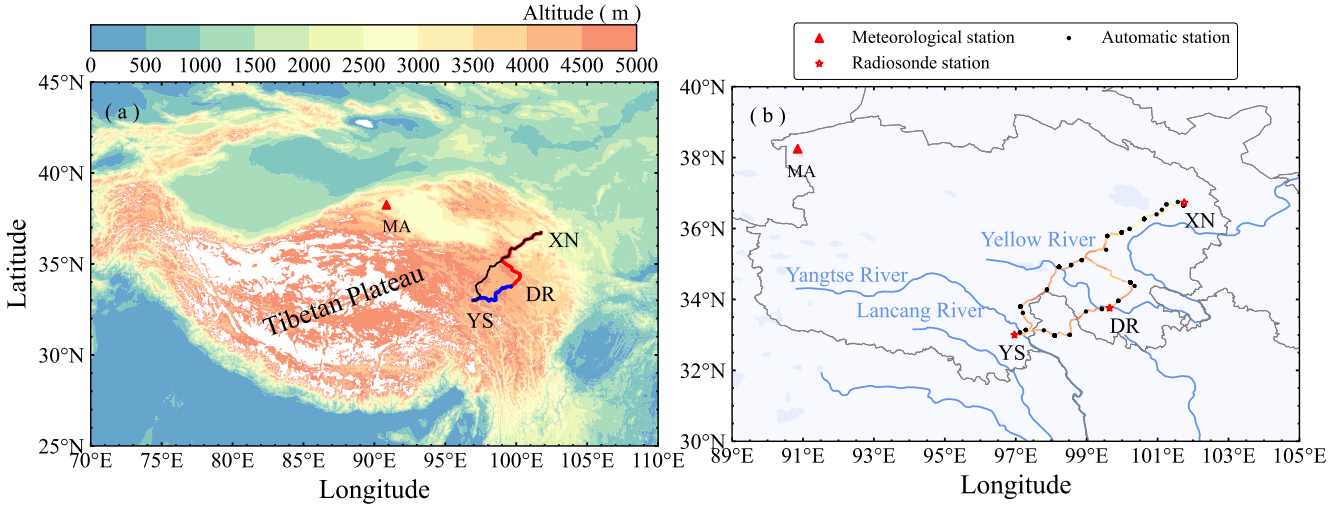

Figure 1. Mobile observation route (**a**) and altitude variation (**b**) in the Three-River-Source Region from 18 to 30 July 2021.

The WP data from radiosonde stations along the MO route were used to validate the inversion accuracy of the wind field and analyze influencing factors. Three radiosonde stations are XN (36.729°N, 101.752°E; 2262 m a.s.l.), DR (33.759°N, 99.647°E; 3968 m a.s.l.), and YS (33.001°N, 96.964°E; 3682 m a.s.l.). There are only two Raobs, at 00:00 and 12:00 UTC, every day. To better evaluate the inversion effect, WP data from the ERA5 reanalysis and inversion model were spatio-temporally matched with the Raobs by taking the average of the data at 23:00 UTC on the previous day and at 00:00 and 01:00 UTC on the same day, as well as the data at 11:00, 12:00, and 13:00 UTC, respectively. These averages were then used to represent the 00:00 and 12:00 UTC WP data. Ultimately, 25 sets of WP data from the ERA5 reanalysis and inversion model were matched with the Raobs.

2.3. LSTM Algorithm

The LSTM network is a variant of the recurrent neural network (RNN) that consists of an input layer, an output layer, and multiple hidden layers.The inclusion of forget gate f_t , input gate i_t, and output gate o_t in the hidden layers regulates the flow of information. By leveraging the gate mechanism, the LSTM network addresses issues such as dependencies, vanishing gradients, and exploding gradients commonly encountered in RNNs [39]. The values of the three "gates" in the LSTM network range between (0, 1), serving the purpose of determining the extent of the preservation of the cell state C_{t-1} from the previous time

step, the level of information retention in the candidate state $\widetilde{C}_t$ at the current time step, and the extent to which the cell state C_t is output to the hidden state h_t .

The recurrent unit structure of LSTM (Figure 2) includes the following calculation process: (1) the input at the current time step x_t and the hidden state of previous time step h_{t-1} are used to compute three "gates" and a candidate state $\widetilde{C}_t$; (2) the forget gate o_t and input gate i_t update the cell state C_t by incorporating the C_{t-1}; (3) the cell state C_t is combined with the output gate o_t to transmit information to the hidden state h_t. The calculation formulas are as follows:

$$\begin{bmatrix} f_t \\ i_t \\ \widetilde{C}_t \\ o_t \end{bmatrix} = \begin{bmatrix} \sigma \\ \sigma \\ tanh \\ \sigma \end{bmatrix} \left(W \begin{bmatrix} x_t \\ h_{t-1} \end{bmatrix} + b \right) \tag{1}$$

$$C_t = f_t * C_{t-1} + i_t * \widetilde{C}_t \tag{2}$$

$$h_t = o_t * tanh(C_t) \tag{3}$$

where W and b are the weight and bias matrices, respectively, σ is the *sigmoid* function, and *sigmoid* and *tanh* are defined as:

$$sigmoid = \frac{1}{1 + e^{-x}} \tag{4}$$

$$tanh = \frac{e^{x} - e^{-x}}{e^{x} + e^{-x}} \tag{5}$$

The LSTM WP inversion model is constructed using the Tensorflow and Keras frameworks on the Python platform. In order to save training time and computational expense, and speed up the convergence of the training model, we set the hidden layer to two layers. The input layer consists of TB data at 22 channels, while the hidden layer is composed of two layers of LSTM networks, one dense layer, and one dropout layer. The output layer represents the WP at 11 vertical heights. The WP inversion process (Figure 3) encompasses essential steps such as data quality control, dataset division, model construction and parameter configuration, WP inversion, and result evaluation. The detailed information of each step is described as follows:

(1) Quality control: if the MOTB at channel i and time j satisfies the expression $\left|TB_{ij} - \overline{TB_i}\right| > 3S_{TB_i}$, it is considered an outlier and needs to be removed. Here, $\overline{TB_i}$ and S_{TB_i} represent the mean and standard deviation of the MOTB for channel i.
(2) Dataset division: the training sets consist of observation TBs at MA station and matching ERA5 reanalysis WP data, while the testing sets consist of MOTB and ERA5 reanalysis WP data.
(3) Model construction and parameter settings: the sequential module is used to build the neural network and initialize the parameters. The time step, output step, dropout, and density are set to 50, 1, 0.5, and 1. The training method is configured through compile. The loss function and optimization algorithm are chosen as MSE and Adam. The number of neurons in the LSTM network, Adam learning rate, batch size, and model iteration count are generated using a random search algorithm and we constructed the best parameter model.
(4) WP inversion: input the testing set features into the best parameter model to obtain the standardized WP and calculate the original value with the mean and standard deviation of WP.
(5) Evaluation of inversion results: assess inversion results using the Raob.

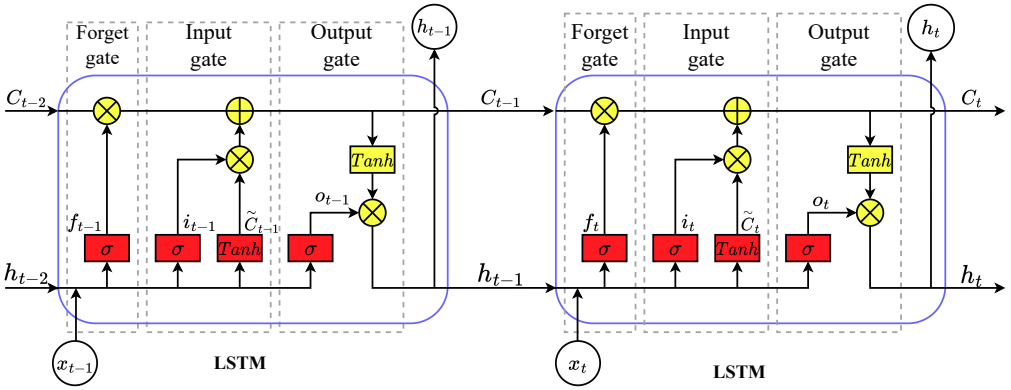

Figure 2. Schematic diagram of the recurrent unit structure of LSTM algorithm.

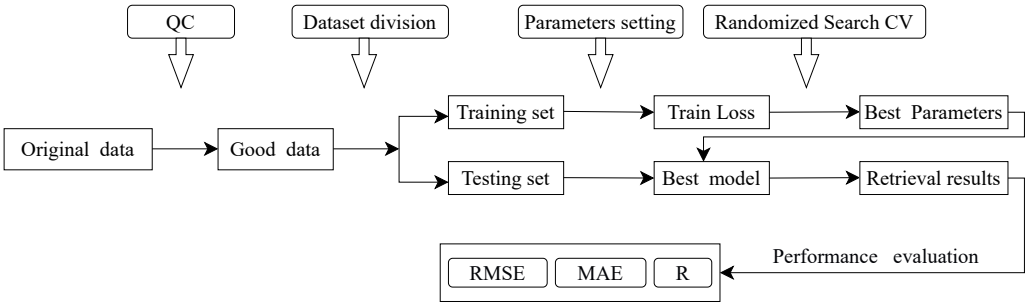

Figure 3. Flowchart of WP retrieval based on LSTM and TB data.

3. TB Verification

The quality of the TB data at each channel directly affects the inversion accuracy of WP, thus we adopted the RTTOV-gb model to indirectly reflect the reliability of MOTB data before the inversion of WP. The RTTOV rapid radiative transfer model (RTM) is developed, maintained, updated, and validated by the European Centre for Medium-Range Weather Forecasts (ECMWF) and has progressed to version 12 [40]. This model is extensively used for simulating the MOTB of spaceborne MR and data assimilation. Evolved from RTTOV v11.2, RTTOV-gb is designed to simulate surface atmospheric radiance ranging from 22 GHz to 150 GHz and is widely used for simulating the TB from GMR [41]. As a parameterized atmospheric RTM, RTTOV-gb can calculate the downward radiation and TB at various channels of the equipment [42].

Before simulating the MOTB over the TRSR from 18 to 30 July 2021, the weather during the MO experiment was categorized into clear-sky, cloudy, and rainy conditions based on measurement data including 26 nearby meteorological stations, ERA5 reanalysis data, and observation records according to the method for the classification of weather conditions [43]. The classification method states that the total cloud cover on a clear (cloudy) day is less (more) than 20%, and the hourly rainfall on rainy days is greater than zero. We used the total cloud cover data from the meteorological station or ERA5 grid point nearest to the MO route and classified the weather conditions. Finally, we obtained 79, 180, and 42 sets of data, respectively. We used the AT, RH, and CLW profiles from the ERA5 reanalysis data as the input for simulated TB (STB) calculations and compared the STB with MOTB values. Figure 4 presents a time series chart of the difference between MOTB and STB at 22 channels under all-weather conditions. Notably, the discrepancy between observations and simulations during rainy conditions is large, with the maximum difference in the water vapor channel and the TB exceeding 200 K. Furthermore, the difference in the water vapor channel is obviously larger than in the oxygen channel. This is primarily due to the attachment of water droplets to the antenna radome during rainy conditions, which predominantly detects atmospheric water vapor near the Earth's surface, resulting in a significant decrease in the performance of the MR under rainy conditions [44,45].

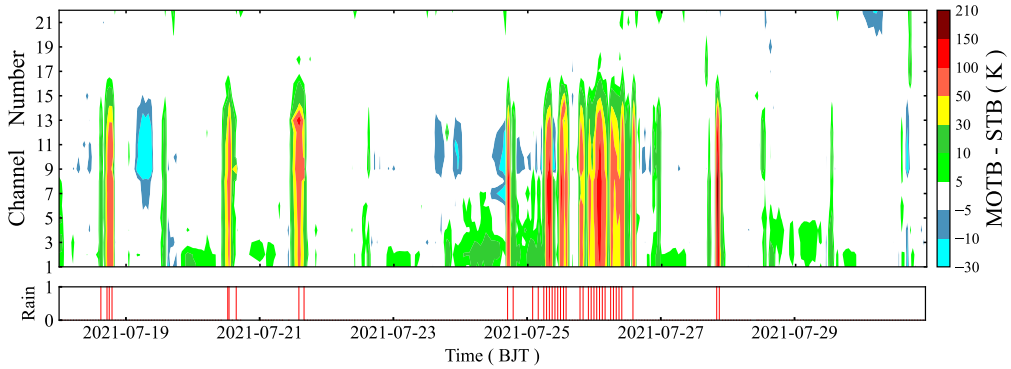

Figure 4. Differences of MOTB and STB at 22 channels under all-weather conditions from 18 to 30 July 2021 (BJT). The red solid line represents the rainy weather process.

Figure 5 presents a comparison between MOTB and STB under different weather conditions. Under the non-precipitation condition, the discrepancy between MOTB and STB decreased remarkably when compared to the rainy condition. The results from Figure 5a indicated that the mean difference (MD) at 22 channels fell between −2 K and 5 K, with the maximum value at the 22.5 GHz and 51.25 GHz channels. Under clear-sky conditions, there are negative deviations at most of the oxygen channels, except for the 54.94 GHz and 56.02 GHz channels, whereas those at the water vapor channels under clear-sky and cloudy conditions are positive. With the exception of individual oxygen channels, most discrepancies under clear-sky conditions are smaller than on cloudy days, mainly because cloud water content, cloud thickness, and cloud height lead to great uncertainty [46–51]. Figure 5b,c show that there is a strong correlation between MOTB and STB under two weather conditions, with correlation coefficients nearing unity. The MD on clear and cloudy days is 0.30 K and 0.78 K, respectively. In general, the MOTBs over the TRSR are reliable under clear-sky and cloudy conditions.

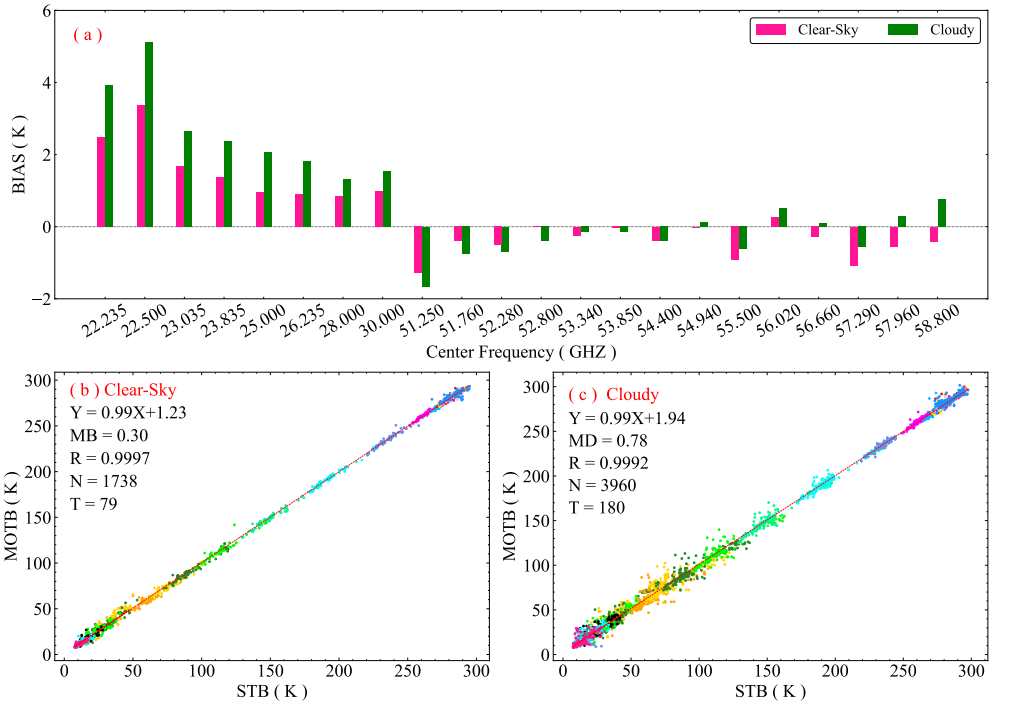

Figure 5. Differences between MOTB and STB at 22 channels and their scatter plots under non-precipitation conditions from July 18 to July 30, 2021 (BJT): (**a**) differences on clear and cloudy days; (**b**) scatter plots on clear days; (**c**) scatter plots on cloudy days. The colourful scatter points represent different channels.

4. Results

4.1. Inversion and Verification

Figure 6 presents scatter plots of WS from the ERA5 reanalysis (hereinafter referred to as Re-WS) and the LSTM inversion model (referred to as In-WS) against Raobs. There is a significant correlation between Re-WS, In-WS, and Raob, with correlation coefficients (R) exceeding 0.96 and passing the 99% confidence level test. The root mean square error (RMSE) and mean absolute error (MAE) were 1.62 m/s and 1.24 m/s for In-WS with Raob, and 1.67 m/s and 1.27 m/s for Re-WS with Raob. In other words, the inversion precision of WS at different heights is slightly better than the ERA5 reanalysis datasets over the TRSR. This may be due to the limited observation data over the TP assimilated into the ERA5 reanalysis datasets, and more MO information used to invert the WP.

Figure 7 presents wind rose plots of wind direction (WD) inverted by the LSTM method (hereinafter referred to as In-WD), WD from the ERA5 reanalysis datasets (hereinafter referred to as Re-WD), and the observation under different WS. Overall, the dominant In-WD and Re-WD are in agreement with the measured WD, and correlation coefficients between In-WD, Re-WD, and measurements both exceed 0.85. The RMSEs of In-WD and Re-WD are quite similar, at 65.15° and 65.72°, respectively. Additionally, differences between In-WD, Re-WD, and observed WD are small under the strong wind conditions, whereas those are large under weak wind scenarios [52].

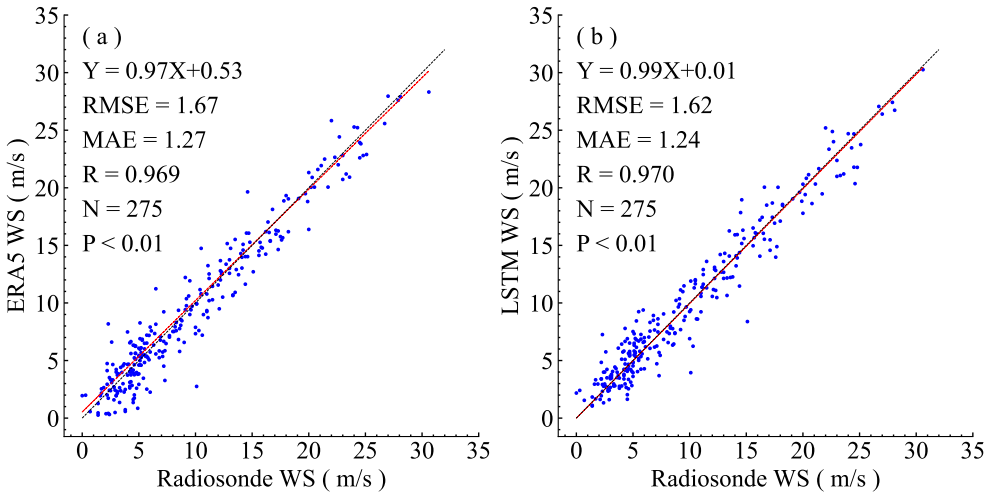

Figure 6. Scatter plots of Re-WS (**a**), In-WS (**b**), and observed WS at XN, DR, and YS radiosonde stations from 18 to 30 July 2021 (BJT). The red and black dashed lines represent the fitting line and the 1:1 reference line, respectively.

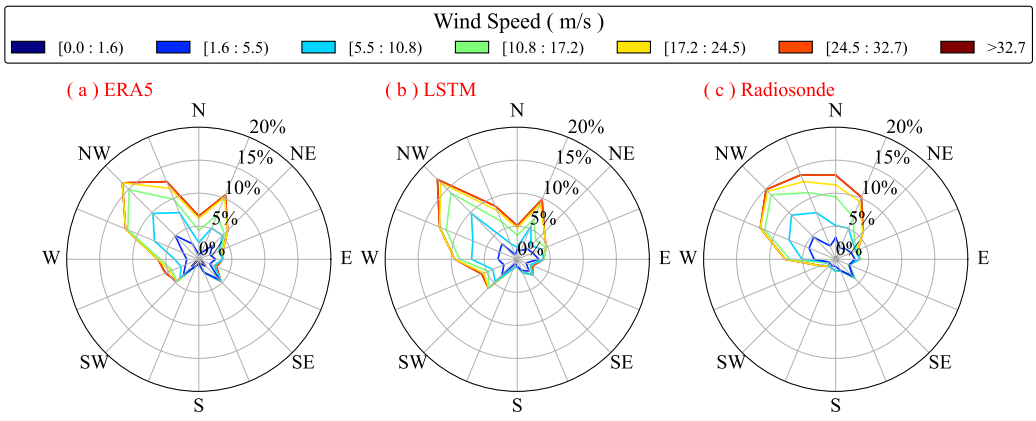

Figure 7. Wind rose plots of observed WD (**c**) at XN, DR, and YS radiosonde stations from 18 to 30 July 2021 (BJT), and corresponding Re-WD (**a**) and In-WD (**b**).

Figure 8 presents the vertical distribution of In-WS, In-WD, Re-WS, Re-WD, Raob, and their RMSEs. The inverted and reanalyzed WS at all heights was consistent with Raob, while the In-WD and Re-WD at 100 hPa, 300 hPa, 350 hPa, and below 450 hPa showed a large deviation. With the exception of the In-WS at 250 hPa, RMSEs of In-WS and Re-WS at all layers are both less than 2 m/s. However, there is a notable discrepancy in the RMSE of In-WD and Re-WD, reaching up to 90° at the heights of 600 hPa and 350 hPa. In general, the RMSE of In-WS and In-WD below 350 hPa is lower than that of Re-WS and Re-WD, whereas the inverse is true above 350 hPa, with increased inversion errors at high atmosphere. It may be related to the weak signal when the vehicle-mounted MR measures the TB using the bottom-up detection approach. In summary, the inverted WS by the MR is reliable, particularly below 350 hPa, although the measurement accuracy of the WD requires further enhancement.

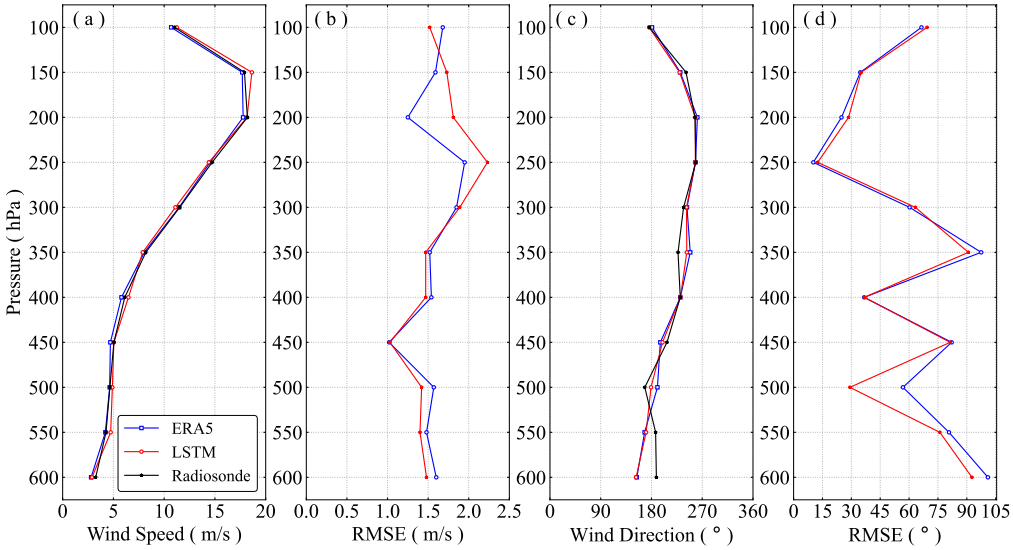

Figure 8. Vertical distribution of In-WS, Re-WS, observed WS (**a**), and that of In-WD, Re-WD, measured WD (**c**), and their RMSEs (**b**,**d**) at XN, DR, and YS radiosonde stations during 18–30 July 2021 (BJT).

4.2. Impact Factors

4.2.1. Weather Conditions

Table 2 presents the RMSE, MAE, R of In-WS, In-WD, and corresponding TB measurement errors under clear-sky, cloudy, and rainy days. The In-WS exhibits a notable correlation with Raob under all-weather conditions, with R surpassing 0.96. The inversion error of WS and WD is the smallest in clear-sky conditions, followed by cloudy conditions, and the largest on rainy days, and is mainly caused by the observation error of TB. The RMSE of In-WS under the three weather conditions is less than 2 m/s, while the In-WD error is relatively large on cloudy and rainy days. Under clear-sky conditions, the inversion errors of WS and WD are smaller, with RMSEs of 1.20 m/s and 26.64°, respectively. The accuracy of WP inversion is significantly affected by cloud coverage, with errors increasing sharply under non-clear conditions. The RMSE of WS reaches 1.75 m/s during rainy conditions, while there is a large discrepancy in In-WD. The differences of WS and WD inversion errors under three weather conditions mainly depend on the measurement errors of TB, and the inversion of WD under non-clear sky conditions needs further improvement in terms of the inversion accuracy by adding information about cloud height and cloud thickness [47]. The main reason for the inversion error differences between WS and WD under the three weather conditions is that the atmospheric composition is relatively stable under clear-sky conditions in the radiative transfer process, and the existence of clouds and raindrops on cloudy and rainy days affects the scattering and absorption of radiation, which increases the uncertainty of the radiative transfer process.

Table 2. Error statistics of In-WS, In-WD, and OTB at XN, DR, and YS radiosonde stations under different weather conditions during 18–30 July 2021 (BJT).

Weather Conditions	Wind Speed (Unit: m/s)			Wind Direction (Unit: °)			TB (Unit: K)	
	RMSE	MAE	R	RMSE	MAE	R	MD	R
Clear-Sky	1.20	0.96	0.98	26.64	15.30	0.97	−0.26	0.9999
Cloudy	1.66	1.26	0.97	66.80	33.31	0.86	0.93	0.9997
Rainy	1.75	1.35	0.97	70.47	42.48	0.81	36.91	0.8466

4.2.2. Altitude Elevation

The atmospheric absorption coefficient curve for microwave bands is related to elevation. Consequently, the altitude is another critical factor for the measurement of TB and the inversion of WP. In consideration of significant uncertainties in MR performance on rainy days, we conducted quality control on 19 sets of observation data under non-precipitation conditions and obtained 17 sets of effective WP data. They are divided into three categories according to the heights of 0∼2.2 km, 2.3∼3.6 km, and 3.7∼4.0 km, with 4, 8, and 5 sets for each group of WPs, respectively. Table 3 presents the RMSE, MAE, R of In-WS, In-WD, and corresponding TB measurement errors at varying altitudes. The MD of OTB and the RMSE of In-WS below an elevation of 4.0 km are less than 1.0 K and 2.0 m/s, respectively. Although the RMSE of WD is larger, the MAE and R are close to 30° and 0.9, respectively. The MD of OTB and the RMSE of In-WS and In-WD increase with altitude, because the density of water vapor and oxygen decreases as the altitude increases, leading to a gradual rise in both TB observation errors and WP inversion errors.

Table 3. Error statistics of In-WS, In-WD, and OTB at XN, DR, and YS radiosonde stations under different altitude conditions during 18–30 July 2021 (BJT).

Altitude	Wind Speed (Unit: m/s)			Wind Direction (Unit: °)			T (Unit: K)	
	RMSE	MAE	R	RMSE	MAE	R	MD	R
0∼2.2 km	1.25	1.05	0.99	40.06	21.35	0.95	0.08	0.9996
2.3∼3.6 km	1.38	1.09	0.98	57.66	25.94	0.88	0.39	0.9997
3.7∼4.0 km	1.93	1.40	0.95	64.60	32.64	0.87	0.86	0.9998

4.2.3. Observation Modes

There are 20 instances of non-precipitation Raobs at XN, DR, and YS radiosonde stations during the MFOCAP. In order to analyze the impact of the observation mode on the inversion accuracy of WP, we classified 20 sets of MOTB, In-WS, and In-WD data into 5 sets of MO and 14 sets of motionless conditions. A comparison of two TBs (Figure 9a,d) revealed a significant correlation between the STB and the MOTB. MDs of MOTB under the MO and stationary conditions were 1.28 K and 0.38 K, respectively. This discrepancy between MOTB and STB is primarily attributed to the impact of vehicular vibrations, inclination, and surrounding obstructions to the measurement performance of the MR when the vehicle was moving. The results in Figure 9 indicated that the inversion accuracy of WS and WD, when the vehicle was motionless, was better than that for the MO scenario. This is consistent with the measured errors in TB. Although the RMSE of the In-WS for the MO condition exceeded 2 m/s, the In-WS below 250 hPa, with WS being less than 15 m/s, were close to the Raob, and the correlation coefficient was larger. Moreover, the RMSE of In-WD under the two observation modes is larger because MO data were measured on cloudy days most of the time. In other words, except for in-situ observation, we can also acquire reliable atmospheric dynamic structural information at the lower atmosphere layer with high spatio-temporal resolution on a large scale using the MR MO mode.

4.2.4. TB Diurnal Variation

In order to investigate the impact of diurnal variation in TB on WP retrieval, TB and WP data during the non-precipitation periods were divided into two categories as follows: data at 08:00 and 20:00 Beijing time (UTC+8), with 10 and 9 observation moments for each category, respectively. Figure 10 presents comparisons of STB and MOTB, and those of In-WS, In-WD, and Raob at two instances. Results showed that the R between STB and MOTB, and those between In-WS and Raobs, are all large, with R exceeding 0.95, while the Rs of In-WD are more different. The difference between STB and MOTB at 08:00 was slightly less than that at 20:00, and the MDs of TB at the two times were both small. The RMSE of In-WS is lower than 2 m/s at both moments, while the difference of In-WD is large. In addition, the RMSEs of In-WS and In-WD at 08:00 were smaller than those at 20:00 and were related to the MD of MOTB.

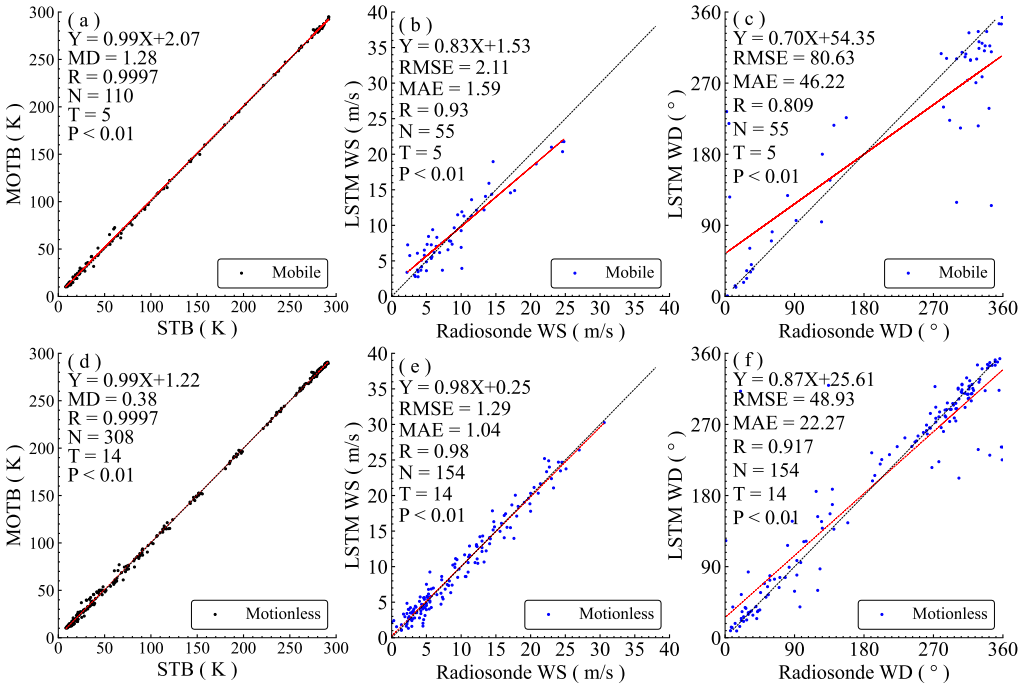

Figure 9. Scatter plots of STB and MOTB, In-WS and measured WS, In-WD and measured WD at 11 atmospheric layers with the mobile (**a**–**c**), and fixed (**d**–**f**) observation mode. Red and black dashed lines represent fitted lines and the 1:1 line.

4.3. Vertical Variation Characteristics of Retrieved WP

The reliability of the retrieved WP and its impact factors were analyzed in the previous sections, but the question remains of how to apply the retrieved WP data with high spatio-temporal resolution to the research and operation of atmospheric dynamic structure? We evaluated the performance of the LSTM approach for reproducing the spatio-temporal evolution features of wind fields and vertical wind shear characteristics. Figure 11 displays the retrieved WP and Raobs at the XN, DR, and YS stations. The results showed that the retrieved WPs at different heights under all-sky conditions are basically consistent with Raobs except for those at rainy times (at 08:00 BJT on 25 July) at XN station. In other words, the LSTM inversion model can reproduce the vertical variation characteristics of wind fields under different weather conditions. On clear days, the LSTM retrieval model can accurately capture the vertical variations of wind fields, while its performance is relatively inferior under cloudy conditions. The weakest reproduction ability is observed on rainy days, particularly at 08:00 BJT on the 25th at the XN station. Under non-precipitation conditions, the LSTM inversion model successfully reproduces the spatio-temporal evolution features of wind fields at all three stations as time progresses.

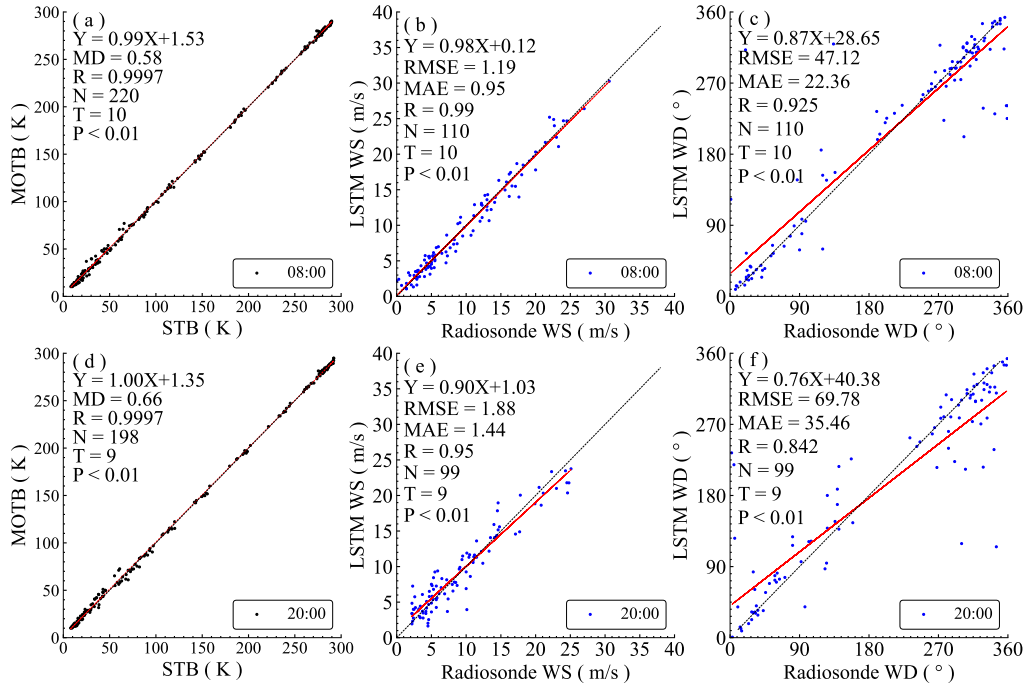

Figure 10. Scatter plots of STB and MOTB, In-WS and measured WS, In-WD and measured WD at 11 atmospheric layers at 08:00 (**a**–**c**) and 20:00 (**d**–**f**) at XN, DR, and YS radiosonde stations from 18 to 30 July 2021 (BJT). The red and black dashed lines represent the fitted line and the 1:1 line.

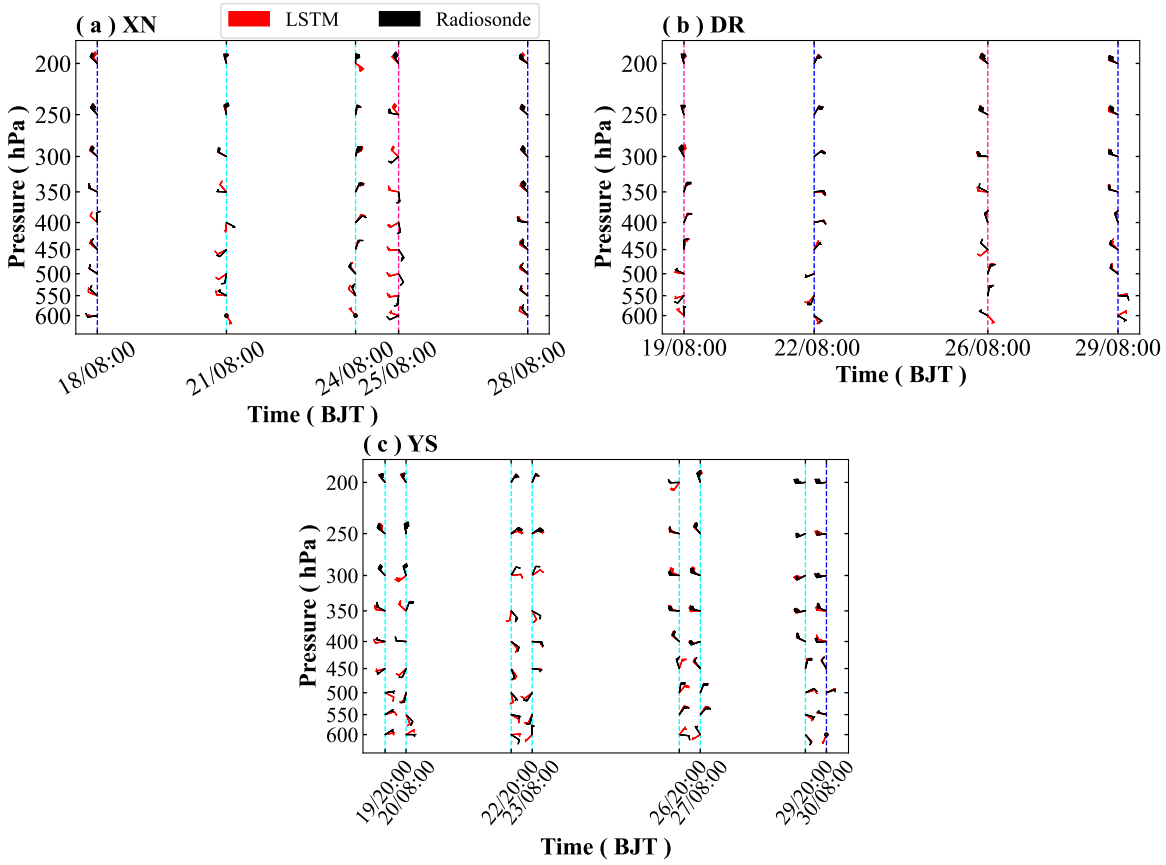

Figure 11. Comparison between the retrieval WP and Raob at XN (**a**), DR (**b**), and YS (**c**) radiosonde stations from 18 to 30 July 2021 (BJT). The blue, cyan, and pink dashed lines represent clear-sky, cloudy, and rainy days.

Two typical low-level vertical wind shears occurred under clear-sky conditions at DR station, as shown in Figure 11b. The Raob at 08:00 BJT on 22 July at DR station revealed a weak vertical wind shear. The southeast wind at the height of 600 hPa gradually changed to a southwest wind between 550 hPa and 500 hPa, followed by a rapid change in WD to the northeast at 450 hPa, and then gradually turned into an easterly or northeasterly wind above 400 hPa. However, there is no significant variation in WS during this process. Similarly, there is a pronounced wind shear feature below 350 hPa at the same station at 08:00 BJT on 29 July, and the WD changes are not notable above 350 hPa. However, the WS gradually increased with altitude. The LSTM inversion model successfully reproduced the variation characteristics of low-level vertical wind shear during the two processes. In general, the LSTM inversion model can capture the temporal-spatial evolution characteristics of WP and vertical wind shear, particularly under clear-sky conditions. Thus, the inversion of WP with the LSTM algorithm has scientific significance for investigating meso-scale atmospheric dynamic structures, vertical wind shear features, atmospheric boundary layer turbulence, the meteorology causes of atmospheric pollution, and improving the assessment and forecasting of wind energy resources.

5. Conclusions

This study utilized a mobile vehicle-mounted MR to collect TB data in the TRSR over the TP from 18 to 30 July 2021. The study proposed a direct inversion method for WP based on the LSTM algorithm, TB data observed at MA stations, and MOTB data collected during the MFOCAP over the TRSR. The reliability of the MOTB was verified, and the influences of weather conditions, altitude, observation mode, and TB diurnal variation on the measurement accuracy of TB and the inversion precision of wind field were analyzed. Furthermore, the ability of the LSTM retrieval method to reproduce the spatio-temporal variations characteristics of WP and vertical wind shear was evaluated.

The reliability of MOTB under different weather conditions was analyzed using the RTTOV-gb model. Rainfall has a significant impact on TB observations, while the optimal performance of the mobile MR under clear-sky conditions is observed. The MD between STB and MOTB for all 22 channels is 0.30 K, whereas it increases to 0.78 K under cloudy conditions.

Based on the TB dataset measured with the GMR at the MA fixed observation station from January to December 2021, as well as the corresponding ERA5 reanalysis datasets, we established an LSTM inversion model of WP to retrieve the vertical wind field data over the TRSR. The inversion accuracy of WP was examined by comparing it with the Raobs at the XN, DR, and YS radiosonde stations. In general, the In-WS below 350 hPa are better than the ERA5 reanalysis datasets, and the dominant retrieved WD and reanalysis WD are agreement with the measured WD.

The observation mode of the MR, weather conditions, altitude, and TB diurnal variation have an impact on TB measurement and WP retrieval. The WS retrieval error under different weather conditions is within 2 m/s, while rainfall has the greatest impact on TB measurement and WS retrieval. The RMSE of In-WS and In-WD on clear days is the smallest, that of the cloudy days takes second place, and that of the rainy days is the largest. The TB measurement and WP inversion with fixed observation mode are better than those under MO. As the altitude increases, errors in TB observation and WP retrieval gradually increase. At the same time, the WP retrieval error at 08:00 is smaller than that at 20:00 BJT.

The LSTM method for the retrieval of WP is capable of reproducing the spatio-temporal evolution characteristics of wind field under clear-sky and cloudy conditions, but there are significant differences in rainy conditions. The LSTM inversion model can capture the temporal-spatial evolution characteristics of WP and vertical wind shear, particularly under clear-sky conditions.

Overall, the LSTM inversion model of WP can provide reliable vertical structure information about the wind field with high spatio-temporal resolution, and capture the temporal-spatial evolution characteristics of WP and vertical wind shear. However, this

study also has some limitations. Firstly, the MA observation station is far away from the MO route, and the poor representativeness and limited training sample of TB data have certain impacts on the inversion of WP. Secondly, because radiosonde stations over the TP are sparse and the temporal resolution is lower, we only used the EAR5 reanalysis data to construct the inversion model. Lastly, the MO experiment over the TRSR has a short observation duration and limited coverage. In order to improve the inversion accuracy of WP, further investigation would be valuable, using the long-term TB and wind field data observed at the same radiosonde station, or more measurements such as cloud cover, cloud height, cloud thickness and so on, and combining the surface and satellite TB observations to reduce the retrieval error of the wind field at the upper atmosphere.

Author Contributions: Conceptualization, X.X., X.C. and B.C.; Methodology, B.C.; Software, X.C., B.C. and Z.H.; Validation, B.C.; Formal analysis, X.C., B.C. and S.M.; Investigation, B.C.; Resources, X.C., D.S., B.C. and S.M.; Data curation, B.C.; Writing—original draft preparation, B.C.; Writing—review and editing, B.C. and X.C.; Visualization, B.C.; Project administration, X.X. and X.C.; Funding acquisition, X.X. and X.C. All authors have read and agreed to the published version of the manuscript.

Funding: This work was supported jointly by the National Natural Science Foundation of China (Grant No. 42375080) and the Fundamental Research Funds for Central Public Interest Scientific Institution from the Chinese Academy of Meteorological Sciences (Grant No. 2021Z013).

Data Availability Statement: ERA5 hourly data for AT, RH, CLW, U, and V wind pressure levels from 1940 to present are publicly available at https://cds.climate.copernicus.eu/cdsapp#!/dataset/reanalysis-era5-pressure-levels?tab=form (accessed on 7 July 2022). The Raob data are publicly available at http://data.cma.cn/ (accessed on 5 October 2022). The TB data derived from this study are available upon request.

Acknowledgments: The authors thank Xuelong Chen from the Institute of Tibetan Plateau Research, Chinese Academy of Sciences for providing the TB data at MA station. We acknowledge Yuxing Yun from Chinese Academy of Meteorological Sciences for providing the revised suggestion.

Conflicts of Interest: The authors declare no conflicts of interest.

Abbreviations

The abbreviation of symbols and their explanation:

Abbreviation	Unit	Remark
TP	-	Tibetan plateau
TRSR	-	Three-River-Source region
Raob	-	Radiosonde observation
MR	-	Microwave radiometer
GMR	-	Ground-based microwave radiometer
TB	K	Brightness temperature
AT	°C	Atmospheric temperature
RH	%	Relative humidity
WVD	g/m^3	Water vapor density
MO	-	Mobile observation
WP	-	Wind profile
CLW	g/m^3	Cloud liquid water
MFOCAP	-	Mobile Field Observation Campaign of Atmospheric Profiles
CMA_GFS	-	Global Forecast System of China Meteorological Administration
LSTM	-	Long short-term memory
RNN	-	Recurrent neural network
MA	-	Mangai (Meteorological station)
XN	-	Xining (Radiosonde station)
DR	-	Dari (Radiosonde station)
YS	-	Yushu (Radiosonde station)
MOTB	K	Mobile observation brightness temperature
STB	K	Simulated brightness temperature

RTM	-	Radiative transfer model
RTTOV-gb	-	Ground-based radiative transfer model for TOVS
ECMWF	-	European Centre for Medium-Range Weather Forecasts
WS	m/s	Wind speed
In-WS	m/s	Inversion of wind speed
Re-WS	m/s	Wind speed from the ERA5 reanalysis
WD	degree (°)	Wind direction
In-WD	degree (°)	Inversion of wind direction
Re-WD	degree (°)	Wind direction from the ERA5 reanalysis
RMSE	-	Root mean square error
MAE	-	Mean absolute error
MD	-	Mean difference
R	-	Correlation coefficient

References

1. Immerzeel, W.W.; Van Beek, L.P.; Bierkens, M.F. Climate change will affect the Asian water towers. *Science* **2010**, *328*, 1382–1385. [CrossRef]
2. Ye, D. Some characteristics of the summer circulation over the Qinghai-Xizang (Tibet) Plateau and its neighborhood. *Bull. Am. Meteorol. Soc.* **1981**, *62*, 14–19.[CrossRef]
3. Tao, S.; Ding, Y.H. Observational evidence of the influence of the Qinghai-Xizang (Tibet) Plateau on the occurrence of heavy rain and severe convective storms in China. *Bull. Am. Meteorol. Soc.* **1981**, *62*, 23–30. [CrossRef]
4. Wu, G.; Zhang, Y. Tibetan Plateau forcing and the timing of the monsoon onset over South Asia and the South China Sea. *Mon. Weather Rev.* **1998**, *126*, 913–927. [CrossRef]
5. Wu, G.; Duan, A.; Liu, Y.; Mao, J.; Ren, R.; Bao, Q.; He, B.; Liu, B.; Hu, W. Tibetan Plateau climate dynamics: Recent research progress and outlook. *Mon. Weather Rev.* **2015**, *2*, 100–116. [CrossRef]
6. Xu, X.; Lu, C.; Shi, X.; Gao, S. World water tower: An atmospheric perspective. *Geophys. Res. Lett.* **2008**, *35*, L20815. [CrossRef]
7. Xu, X.; Zhao, T.; Lu, C.; Guo, Y.; Chen, B.; Liu, R.; Li, Y.; Shi, X. An important mechanism sustaining the atmospheric "water tower" over the Tibetan Plateau. *Atmos. Chem. Phys.* **2014**, *14*, 11287–11295. [CrossRef]
8. Duan, A.; Wu, G. Change of cloud amount and the climate warming on the Tibetan Plateau. *Geophys. Res. Lett.* **2006**, *33*, 408. [CrossRef]
9. Duan, A.; Wu, G.; Liu, Y.; Ma, Y.; Zhao, P. Weather and climate effects of the Tibetan Plateau. *Adv. Atmos. Sci.* **2012**, *29*, 978–992. [CrossRef]
10. Chen, G.; Zhang, X.; Fu, Y. Diurnal Variation in Clouds and Radiative Budgets Over the Tibetan Plateau During Summer Using CERES Data. *J. Geophys. Res. Atmos.* **2022**, *127*, e2021JD036329. [CrossRef]
11. Li, L.; Zhang, R.; Jia, L. Climatic characteristics of Tibetan Plateau vortex precipitation based on observations. *Int. J. Climatol.* **2022**, *42*, 9237–9252. [CrossRef]
12. Ma, Y.; Zhong, L.; Su, Z.; Ishikawa, H.; Menenti, M.; Koike, T. Determination of regional distributions and seasonal variations of land surface heat fluxes from Landsat-7 Enhanced Thematic Mapper data over the central Tibetan Plateau area. *J. Geophys. Res. Atmos.* **2006**, *111*, D10305. [CrossRef]
13. Ueno, K.; Fujii, H.; Yamada, H.; Liu, L. Weak and frequent monsoon precipitation over the Tibetan Plateau. *J. Meteorol. Soc. Jpn. Ser. II* **2001**, *79*, 419–434. [CrossRef]
14. Yang, K.; Pinker, R.T.; Ma, Y.; Koike, T.; Wonsick, M.M.; Cox, S.J.; Zhang, Y.; Stackhouse, P. Evaluation of satellite estimates of downward shortwave radiation over the Tibetan Plateau. *J. Geophys. Res. Atmos.* **2008**, *113*, D17204. [CrossRef]
15. Zhao, P.; Xu, X.; Chen, F.; Guo, X.; Zheng, X.; Liu, L.; Hong, Y.; Li, Y.; La, Z.; Peng, H.; et al. The third atmospheric scientific experiment for understanding the earth–atmosphere coupled system over the Tibetan Plateau and its effects. *Bull. Am. Meteorol. Soc.* **2018**, *99*, 757–776. [CrossRef]
16. Westwater, E.R. *Ground-Based Microwave Remote Sensing of Meteorological Variables*, 3rd ed.; Atmospheric remote sensing by microwave radiometry; John Wiley & Sons, Inc.: Hoboken, NJ, USA, 1993; pp. 145–213.
17. Ware, R.; Carpenter, R.; Güldner, J.; Liljegren, J.; Nehrkorn, T.; Solheim, F.; Vandenberghe, F. A multichannel radiometric profiler of temperature, humidity, and cloud liquid. *Radio Sci.* **2003**, *38*, 44-1–44-13.
18. Knupp, K.; Coleman, T.; Phillips, D.; Ware, R.; Cimini, D.; Vandenberghe, F.; Vivekanandan, J.; Westwater, E. Ground-based passive microwave profiling during dynamic weather conditions. *J. Atmos. Ocean. Technol.* **2009**, *26*, 1057–1073. [CrossRef]
19. Madhulatha, A.; Rajeevan, M.; Venkat Ratnam, M.; Bhate, J.; Naidu, C. Nowcasting severe convective activity over southeast India using ground-based microwave radiometer observations. *J. Geophys. Res. Atmos.* **2013**, *118*, 1–13. [CrossRef]
20. Walbröl, A.; Crewell, S.; Engelmann, R.; Orlandi, E.; Griesche, H.; Radenz, M.; Hofer, J.; Althausen, D.; Maturilli, M.; Ebell, K. Atmospheric temperature, water vapour and liquid water path from two microwave radiometers during MOSAiC. *Sci. Data* **2022**, *9*, 534. [CrossRef]
21. Serafin, R.J.; Szejwach, G.; Phillips, B.B. Applications of airborne remote sensing in atmospheric sciences research. *J. Geophys. Res. Ocean.* **1986**, *91*, 2510–2516. [CrossRef]

22. Huggins, A.W. Mobile Microwave Radiometer Observations: Spatial Characteristics of Supercooled Cloud Water and Cloud Seeding Implications. *J. Appl. Meteorol. Climatol.* **1995**, *34*, 432–446. [CrossRef]
23. Karan, H.; Knupp, K. Mobile Integrated Profiler System (MIPS) observations of low-level convergent boundaries during IHOP. *Mon. Weather. Rev.* **2006**, *134*, 92–112. [CrossRef]
24. Wei, C.; Xin, M.; Wang, P. Analysis of Precipitable Water and Cloud Liquid Water Content over Equatorial Area of Western Pacific Basis of Remote Sensing. *Chin. J. Atmos. Sci.* **1992**, *164*, 1–10.
25. Chen, H.; Lu, D.; Wei, C.; Liu, J. Comparison of the Effects of Different Microwave Channel Combinations and TB Functions in the Algorithm for Retrieving Precipitable Water in the Clear Atmosphere. *Chin. J. Atmos. Sci.* **1996**, *20*, 757–762.
26. Cheng, X.; Xu, X.; Bai, G.; Wang, R.; Ma, J.; Zhang, L.; Su, D.; Chen, B.; Ma, S.; Hu, C.; et al. Mobile Observation Field Experiment of Atmospheric Vertical Structure And Its Contribution to Precipitation Forecasts Over the Tibet Plateau. *JGR-Atmospheres* 2023, *revised*.
27. Bu, J.; Yu, K.; Zuo, X.; Ni, J.; Li, Y.; Huang, W. GloWS-Net: A Deep Learning Framework for Retrieving Global Sea Surface Wind Speed Using Spaceborne GNSS-R Data. *Remote Sens.* **2023**, *15*, 590. [CrossRef]
28. Shi, X.; Duan, B.; Ren, K. F2F-NN: A Field-to-Field Wind Speed Retrieval Method of Microwave Radiometer Data Based on Deep Learning. *Remote Sens.* **2022**, *14*, 3517.[CrossRef]
29. Ouyed, A.; Smith, N.; Zeng, X.; Galarneau, T., Jr.; Su, H.; Dixon, R.D. Global Three-Dimensional Water Vapor Feature-Tracking for Horizontal Winds Using Hyperspectral Infrared Sounder Data From Overlapped Tracks of Two Satellites. *Geophys. Res. Lett.* **2023**, *50*, e2022GL101830. [CrossRef]
30. Ma, Z.; Li, J.; Han, W.; Li, Z.; Zeng, Q.; Menzel, W.P.; Schmit, T.J.; Di, D.; Liu, C.Y. Four-dimensional wind fields from geostationary hyperspectral infrared sounder radiance measurements with high temporal resolution. *Geophys. Res. Lett.* **2021**, *48*, e2021GL093794.[CrossRef]
31. Dietz, A.J.; Kuenzer, C.; Gessner, U.; Dech, S. Remote sensing of snow—A review of available methods. *Int. J. Remote Sens.* **2012**, *33*, 4094–4134. [CrossRef]
32. Smagulova, K.; James, A.P. A survey on LSTM memristive neural network architectures and applications. *Eur. Phys. J. Spec. Top.* **2019**, *228*, 2313–2324. [CrossRef]
33. Jiang, C.; Li, D.; Wang, D.; Zhang, L. Quantification and assessment of changes in ecosystem service in the Three-River Headwaters Region, China as a result of climate variability and land cover change. *Ecol. Indic.* **2016**, *66*, 199–211. [CrossRef]
34. Cai, Y.; Luo, S.; Wang, J.;Qi, D.; Hu, X. Spatiotemporal variations in precipitation in the Three-River Headwater region from 1961 to 2019. *Pratacultural Sci.* **2022**, *39*, 10–20.
35. Meng, X.H.; Chen, H.; Li, Z.; Zhao, L.; Zhou, B.; Lv, S.H.; Deng, M.S.; Liu, Y.M.; Li, G.W. Review of climate change and its environmental influence on the Three-River Regions. *PLateau Meteorol* **2020**, *39*, 1133–1143.
36. Liang, L.; Li, L.; Liu, C.; Cuo, L. Climate change in the Tibetan plateau three rivers source region: 1960–2009. *Int. J. Climatol.* **2013**, *33*, 2900–2916. [CrossRef]
37. Ma, Y.; Yao, T.; Zhong, L.; Wang, B.; Xu, X.; Hu, Z.; Ma, W.; Sun, F.; Han, C.; Li, M.; et al. Comprehensive study of energy and water exchange over the Tibetan Plateau: A review and perspective: From GAME/Tibet and CAMP/Tibet to TORP, TPEORP, and TPEITORP. *Earth-Sci. Rev.* **2019**, *237*, 104312. [CrossRef]
38. Chen, X.; Ma, Y.; Wang, B.; Xu, X.; Cheng, X.; Liu, Y.; Xu, X.; Li, L.; Ma,W. TP-PROFILE monitoring the thermodynamical structure of the troposphere over the Third Pole. *Adv. Atmos. Sci.* 2023, *in press*. [CrossRef]
39. Yu, Y.; Si, X.; Hu, C.; Zhang, J. A review of recurrent neural networks: LSTM cells and network architectures. *Neural Comput.* **2019**, *31*, 1235–1270. [CrossRef]
40. Saunders, R.; Hocking, J.; Turner, E.; Rayer, P.; Rundle, D.; Brunel, P.; Vidot, J.; Roquet, P.; Matricardi, M.; Geer, A.; et al. An update on the RTTOV fast radiative transfer model (currently at version 12). *Geosci. Model Dev.* **2018**, *11*, 2717–2737. [CrossRef]
41. De Angelis, F.; Cimini, D.; Hocking, J.; Martinet, P.; Kneifel, S. RTTOV-gb–adapting the fast radiative transfer model RTTOV for the assimilation of ground-based microwave radiometer observations. *Geosci. Model Dev.* **2016**, *9*, 2721–2739. [CrossRef]
42. Cimini, D.; Hocking, J.; De Angelis, F.; Cersosimo, A.; Di Paola, F.; Gallucci, D.; Gentile, S.; Geraldi, E.; Larosa, S.; Nilo, S.; et al. RTTOV-gb v1. 0–updates on sensors, absorption models, uncertainty, and availability. *Geosci. Model Dev.* **2019**, *12*, 1833–1845. [CrossRef]
43. Cheng, X.; Su, D.; Li, D.; Chen, L.; Xu, W.; Yang, M.; Li, Y.; Yue, Z.; Wang, Z. An improved method for correction of air temperature measured using different radiation shields. *Adv. Atmos. Sci.* **2014**, *31*, 1460–1468.[CrossRef]
44. Ware, R.; Cimini, D.; Herzegh, P.; Marzano, F.; Vivekanandan, J.; Westwater, E. Ground-based microwave radiometer measurements during precipitation. In Proceedings of the 8th Specialist Meeting on Microwave Radiometry, Rome, Italy, 24–27 February 2004; pp. 24–27.
45. Araki, K.; Murakami, M.; Ishimoto, H.; Tajiri, T. Ground-based microwave radiometer variational analysis during no-rain and rain conditions. *Sola* **2015**, *11*, 108–112. [CrossRef]
46. Ahn, M.H.; Won, H.; Han, D.; Kim, Y.H.; Ha, J.C. Characterization of downwelling radiance measured from a ground-based microwave radiometer using numerical weather prediction model data. *Atmos. Meas. Tech.* **2016**, *9*, 281–293. [CrossRef]
47. Li, Q.; Wei, M.; Wang, Z.; Jiang, S.; Chu, Y. Improving the Retrieval of Cloudy Atmospheric Profiles from Brightness Temperatures Observed with a Ground-Based Microwave Radiometer. *Atmosphere* **2021**, *12*, 648.[CrossRef]

48. Liu, M.; Liu, Y.A.; Shu, J. Characteristics Analysis of the Multi-Channel Ground-Based Microwave Radiometer Observations during Various Weather Conditions. *Atmosphere* **2022**, *13*, 1556. [CrossRef]
49. Che, Y.; Ma, S.; Yang, L. Cloud influence on atmospheric humidity profile retrieval by ground-based microwave radiometer. *J. Appl. Meteor. Sci.* **2015**, *26*, 193–202. [CrossRef]
50. Wang, Z.; Zhang, X.; Mao, J. Comparison analysis on detection performance of ground-based microwave radiometers under different weather conditions. *J. Appl. Meteor. Sci.* **2018**, *29*, 282–295.[CrossRef]
51. Xing, Y.; Lou, G.; Li, X.; Zhang, G. Influence of cloudy and rainy weather on the brightness of the sky in the 3mm wavelength band. *Mod. Def. Technol.* **2010**, *5*, 82–85.
52. Radinović, D.; Ćurić, M. Measuring scales for daily temperature extremes, precipitation and wind velocity. *Meteorol. Appl.* **2014**, *21*, 461–465. [CrossRef]